ResearchGate

See discussions, stats, and author profiles for this publication at: https://www.researchgate.net/publication/228688215

Optical Spectroscopy of Eu3+ Doped ZnO Nanocrystals

ARTICLE *in* THE JOURNAL OF PHYSICAL CHEMISTRY C · JANUARY 2008

Impact Factor: 4.77 · DOI: 10.1021/jp077001z

CITATIONS
106

READS
95

6 AUTHORS, INCLUDING:

Yongsheng Liu
China University of Petroleum
188 PUBLICATIONS **3,739** CITATIONS
SEE PROFILE

Wenqin Luo
Chinese Academy of Sciences
39 PUBLICATIONS **1,078** CITATIONS
SEE PROFILE

Renfu Li
Chinese Academy of Sciences
54 PUBLICATIONS **1,666** CITATIONS
SEE PROFILE

G. K. Liu
Argonne National Laboratory
162 PUBLICATIONS **2,585** CITATIONS
SEE PROFILE

Available from: G. K. Liu
Retrieved on: 24 January 2016

Optical Spectroscopy of Eu^{3+} Doped ZnO Nanocrystals

Yongsheng Liu,[†] Wenqin Luo,[†] Renfu Li,[†] Guokui Liu,[‡] Mark R. Antonio,[‡] and Xueyuan Chen*,[†]

State Key Laboratory of Structural Chemistry, Key Laboratory of Optoelectronic Materials Chemistry and Physics, Fujian Institute of Research on the Structure of Matter, Chinese Academy of Sciences, Fuzhou, Fujian 350002, China, and Chemistry Division, Argonne National Laboratory, Argonne, Illinois 60439

Received: August 31, 2007; In Final Form: October 21, 2007

The energy levels and local structures of Eu^{3+} incorporated in the lattice and surface sites of ZnO nanocrystals were investigated based on the high-resolution fluorescence spectra at 10 K. Radiative emissions from $^5D_1$ were first observed for Eu^{3+} at the lattice site of ZnO. It is shown that the site symmetry of Eu^{3+} at the lattice site descends from C_{3v} to C_s or C_1, whereas Eu^{3+} ions at the surface occupy more disordered sites of the lowest symmetry C_1. The luminescence decay of $^5D_0$ at the lattice site, showing a rise time and longer lifetime, behaves distinctly from that of the surface sites. Because of a small filling factor (52%) of nanoparticles, the $^5D_0$ lifetime of Eu^{3+} is significantly affected by the surrounding medium, which can be well interpreted with the virtual-cavity model. The Judd−Ofelt intensity parameters of Eu^{3+} in ZnO nanocrystals were determined, with $\Omega_{2,4,6}$ values of (9.59, 8.11, <0.25) and (21.51, 2.30, <0.25) in units of 10^{-20} cm^2 for Eu^{3+} at the surface and lattice sites, respectively. A defect-mediated energy transfer from the ZnO band gap to Eu^{3+} was observed. The growth mechanism for the incorporation of Eu^{3+} into the ZnO lattice was also revealed.

1. Introduction

Recently, rare-earth (RE) ion doped semiconductors have been the focus of numerous investigations because of their unique optical properties and promising applications in optoelectronic devices.[1−10] One of the advantages offered by these materials is that multicolor light of RE ions could be generated directly from electrical current, for instance, in full color or monochromatic displays. The electronic structure of small semiconductor nanoparticles may be very different from that of the bulk counterparts because of the quantum confinement effect, which thus affects the luminescence dynamics of an optical activator incorporated in such a host. It is anticipated that the luminescence of RE ions incorporated in the semiconductor lattice could be sensitized efficiently by exciton recombination in the host. In this sense, the luminescence of RE ions depends critically on their doping locations in the host. Particularly, ZnO is a well-known wide band gap semiconductor and a good candidate as a host material for RE ions because of its outstanding optical properties. However, because of the different chemical properties between trivalent RE ions and the cations of ZnO, it is rather difficult to incorporate RE ions into the lattice of semiconductors effectively via a wet chemical method. The existence of intrinsic self-purification processes could hamper the introduction of impurities at the nanoscale.[11,12] Although, it is controversial whether RE ions could be incorporated into the II−VI semiconductor lattice,[13] many important results have been achieved.[8,14−20] These results indicated that trivalent RE ions can be introduced into the nanocrystals and energy transfer from the host to RE ions can be achieved if the synthesis method is well-designed and the charge imbalance is intentionally compensated. For instance, Wang et al. observed well-resolved emission lines due to crystal-field (CF) splitting in the visible upconversion spectra of Er^{3+} in ZnO nanocrystals,[14] which might prove that Er^{3+} ions were incorporated into the ZnO lattice. Ishizumi and Kanemitsu observed an energy transfer from ZnO defects to Eu^{3+} in Eu^{3+}:ZnO nanorods fabricated by the microemulsion method.[15] Pereira et al. reported that Tb^{3+} ions could be incorporated into ZnO nanocrystals using colloidal synthetic procedures.[17] More recently, we have provided spectroscopic evidence for the incorporation of Eu^{3+} ions in the lattice of ZnO nanocrystals.[20] So far, optical spectroscopy of Eu^{3+} incorporated in ZnO nanocrystals, such as CF analysis, Judd−Ofelt (JO) intensity calculation, and luminescence dynamics, has not been reported. A comprehensive investigation of these aspects might gain more insight into the understanding of optical behaviors of RE ions in semiconductor nanocrystals, which is of great importance to further material applications.

In this work, CF levels of Eu^{3+} at multiple sites were determined based on high-resolution excitation and emission spectra at low temperature. The local structure, site symmetry, luminescence lifetime, and Judd−Ofelt (JO) intensity parameters of Eu^{3+} at the surface and lattice sites are investigated in detail. Furthermore, the mechanisms of host-to-Eu^{3+} energy transfer and multisite formation are also proposed.

2. Experimental Section

2.1. Nanoparticle Synthesis. Eu^{3+} doped ZnO nanocrystals were synthesized according to a modified sol−gel method.[14,21,22] A mixture of 0.01 mol zinc acetate dihydrate (AR) and europium acetate hexahydrate (99.995%) with a nominal molar ratio of Eu/Zn varied from 0.5 to 4 atom % was dried at 120 °C to remove the water and then transferred into a 250 mL round-bottom flask. Meanwhile, 100 mL of absolute ethanol was added to the round-bottom flask. The mixture was refluxed under vigorous stirring in an 80 °C water bath for 3 h. After this procedure, a clear −Zn−O−Eu− and −Zn−O−Zn− precursor

* Corresponding author. Phone and fax: +86-591-8764-2575. E-mail: xchen@fjirsm.ac.cn.
[†] Fujian Institute of Research on the Structure of Matter, Chinese Academy of Sciences.
[‡] Argonne National Laboratory.

10.1021/jp077001z CCC: $40.75 © 2008 American Chemical Society
Published on Web 01/03/2008

solution was obtained and then cooled to 0 °C immediately. The precursor solution was hydrolyzed by the addition of 0.025 mol of lithium hydroxide monohydrate powder in an ultrasonic bath for 30 min at 0 °C. The introduction of Li^+ was aimed to compensate the charge imbalance between Zn^{2+} and Eu^{3+} in the ZnO lattice. The obtained mixture was precipitated by the addition of adequate hexane. The finally obtained precipitates were isolated by centrifugation, washed with ethanol several times, and dried for 12 h at 40 °C to get the as-grown sample. For better crystallinity and enhanced luminescence, the as-grown samples were further annealed in air for 30 min at 200, 300, and 400 °C, respectively, to get the final products. The final products were white powders with a yield of ~77% based on the starting materials.

2.2. Measurements. The concentrations of Eu^{3+} and Li^+ in Eu^{3+}:ZnO nanocrystals were determined by the Ultima2 ICP optical emission spectrometer. The morphology and chemical compositions of Eu^{3+}:ZnO nanocrystals were investigated by a JEOL-2010 transmission electron microscope (TEM) equipped with the energy-dispersive X-ray spectrum, and a JSM6700F scanning electron microscope (SEM). Powder X-ray diffraction (XRD) patterns were collected using a PANalytical X'Pert PRO powder diffractometer with Cu $K\alpha_1$ radiation ($\lambda = 0.154187$ nm). The UV/vis diffuse reflectance spectra of Eu^{3+} doped ZnO nanocrystals were measured by a Perkin-Elmer Lambda 900 UV/vis/NIR spectrometer using $BaSO_4$ as a blank. The emission and excitation spectra and transient decays were recorded on an Edinburgh Instruments FLS920 spectrofluorimeter equipped with both continuous (450 W) and pulsed xenon lamps. For low-temperature measurements, samples were mounted on a closed cycle cryostat (10−350 K, DE202, Advanced Research Systems). For site-selective spectroscopy, the excitation (or emission) monochromator's slits were set as small as possible to improve the instrumental resolution. The best wavelength resolution is 0.05 nm. The line intensities and positions of the measured spectra were calibrated according to the FLS920 correction curve and standard mercury lamp. The extended X-ray absorption fine structure (EXAFS) spectra were measured at the Advanced Photon Source beam line 12-BM-B[23] (Argonne National Laboratory) using a 13-element fluorescence detector (Canberra). The Eu L_3-edge data were obtained under ambient conditions for powders pressed into micro X-ray cells (SPEX 3577) with Kapton film windows, 0.0003 (SPEX 3511). The data from three 1-h scans of both the as prepared (1.05 atom % Eu) and annealed (400 °C) samples were averaged for analysis, which was performed in consistent fashion in the usual manner[24] with EXAFSPAK.[25] The conventional metrical analysis of the Eu $k^3\chi(k)$ EXAFS with a fixed scale factor ($S_0^2 = 1$) entailed a series of stepwise fits of increasing complexity, from single- to multishell coordination models as well as best-Z searches of distant interactions (Eu−X for X ≡ O, Zn, Eu), using theoretical phase and amplitude functions calculated with FEFF8.0.[26] Ultimately, the EXAFS spectra for both samples were modeled successfully with two-shell fits that included contributions from the nearest O atoms and the distant neighbors—identified as Zn—about Eu. Seven parameters were refined, including Eu−O and Eu−Zn interatomic distances; O and Zn coordination numbers; Eu−O and Eu−Zn Debye−Waller factors; energy threshold parameter, ΔE_0. The number of variables (7) was less than the number of relevant independent data points, $N_I = 9$, available in the primary spectra, $k_{max} = 11.5$ Å^{-1}.[27]

3. Results and Discussion

3.1. Structural and Morphology Characterization. The precise contents of Eu^{3+} and Li^+ were, respectively, determined to be 1.05 ± 0.02 and 4.50 ± 0.09 atom % for the sample doped with a nominal Eu^{3+} content of 1.25 atom % by the Ultima2 ICP optical emission spectrometer. The XRD patterns of Eu^{3+}:ZnO (1.05 atom %) nanoparticles annealed at various temperatures can be indexed to be ZnO with hexagonal wurtzite structure (Figure S1 in the Supporting Information). The XRD patterns indicate the presence of highly crystalline ZnO nanocrystals without any other additional crystalline phase such as Eu_2O_3. By means of the Debye−Scherrer equation, the average sizes of the nanoparticles heated at 40, 200, 300, and 400 °C are estimated to be 5, 8, 9, and 11 nm, respectively. Specifically, for the sample annealed at 400 °C, it is observed that the nanocrystal size is slightly reduced with the increase of Eu^{3+} content, possibly due to the fact that Eu^{3+} ions on the surface or interstitials of ZnO nanocrystals restrain the nanocrystal growth to some extent. A similar phenomenon was observed for Eu^{3+} doped TiO_2 nanocrystals.[28]

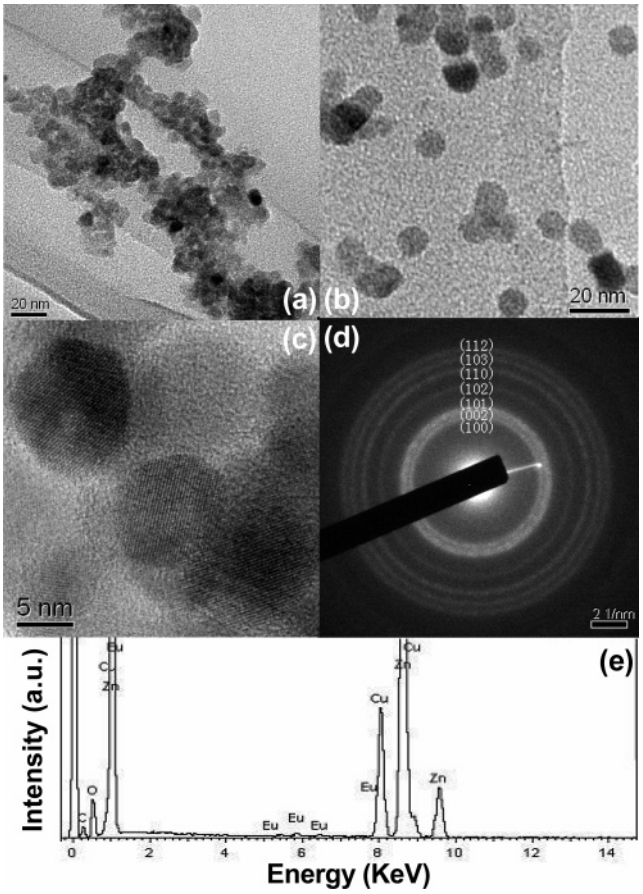

Figure 1. TEM images and SAED and EDS patterns of Eu^{3+}:ZnO (1.05 atom %) nanocrystals: (a) TEM image of the as-grown nanocrystals; (b) TEM and (c) HRTEM images of nanoparticles annealed at 400 °C; (d) SAED and (e) EDS patterns of nanoparticles annealed at 400 °C.

Figure 1 compares the TEM images of Eu^{3+}:ZnO (1.05 atom %) nanocrystals before and after annealing at 400 °C. The as-grown nanoparticles are irregularly spherical with a diameter of ~5 nm and tend to aggregate (Figure 1a), whereas the annealed nanoparticles are well-crystallized with a diameter of ~10 nm (Figure 1b), the sizes of which agree well with their XRD estimates. As shown in the high-resolution TEM image (HRTEM) in Figure 1c, the crystalline lattice fringes of ZnO are very clear, indicating that the annealed nanoparticles possess higher crystallinity. The selected area electron diffraction (SAED) rings of the annealed nanoparticles in Figure 1d exhibit the polycrystalline nature, and can be well-indexed to diffrac-

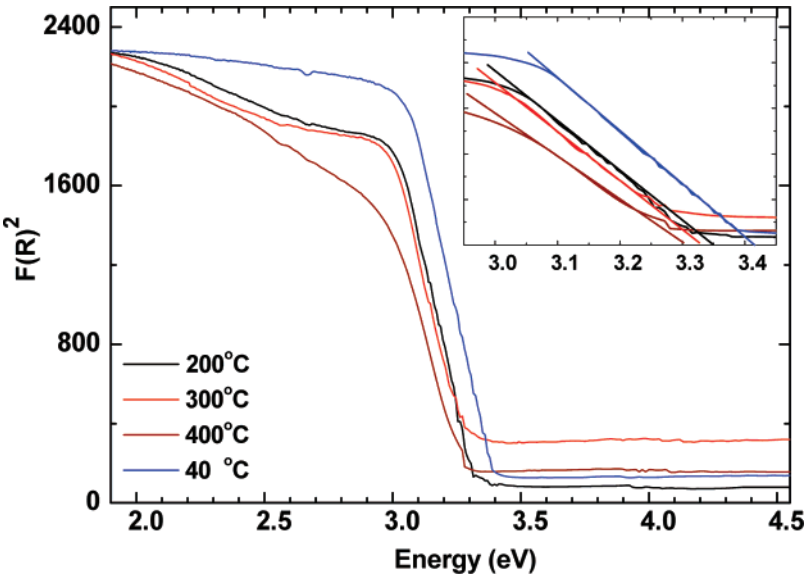

Figure 2. Plot of $F(R)^2$ vs photon energy for direct transition of Eu^{3+}:ZnO (1.05 atom %) nanocrystals annealed at different temperatures. $F(R)$ is the Kubelka−Munk function, with $F(R) = (1 - R)^2/2R$, and R is the reflectance. Band gap energies, E_g, are obtained by extrapolation to $F(R) = 0$.

tions from the (100), (002), (101), (102), (110), (103), and (112) planes of the hexagonal wurtzite structure in turn, which are in good agreement with the XRD patterns. The energy-dispersive X-ray spectrum (EDS) of the annealed nanoparticles in Figure 1e confirms the presence of a small amount of Eu in ZnO nanocrystals. No Li is detected because of its rather small atomic weight.

The UV−visible reflectance spectra of Eu^{3+}:ZnO (1.05 atom %) nanocrystals with different sizes are measured. Figure 2 shows plots of $F(R)^2$ versus photon energy $h\nu$ for Eu^{3+}:ZnO (1.05 atom %) annealed at different temperatures, where $F(R)$ is the Kubelka−Munk function,[29] with $F(R) = (1 - R)^2/2R$ and R is the observed reflectance in UV/vis spectra. All samples show strong absorption with a steep onset around 3.0 eV corresponding to the excitonic $1S_h \rightarrow 1S_e$ transition of ZnO. By adopting the method proposed by Cao et al.,[30] the band gap energies (E_g) of the samples heated at 40, 200, 300, and 400 °C (with sizes of 5, 8, 9, and 11 nm,respectively) are determined to be 3.41, 3.35, 3.33, and 3.30 eV by the extrapolation to $F(R) = 0$. The obtained band gap energy of Eu^{3+}:ZnO nanocrystals shifts to the blue with the decrease in size due to the quantum confinement effect.[31,32] An increase of ~0.11 eV is observed as the nanoparticle size decreases from 11 to 5 nm. Similarly, based on the absorption spectra, Wang et al. observed an increase of ~0.10 eV when the size of ZnO decreased from 6.4 to 3.9 nm.[31] A small peak centered at 2.67 eV for samples heated at 40 and 200 °C is observed in Figure 2, which may be assigned to the $^7F_0 \rightarrow {}^5D_2$ transition of Eu^{3+} as usually observed in the absorption spectrum of Eu^{3+}.

3.2. Crystal-Field Levels of Eu^{3+}. Recently, we have shown the existence of multiple sites of Eu^{3+} incorporated in 9-nm ZnO (1.6 atom %) nanocrystals, and two sites denoted as sites A and B were resolved.[20] In fact, such a multisite structure can be observed for Eu^{3+} with a doping content from 0.5 to 4.0 atom % (Figure S2 in the Supporting Information). To date, no detailed optical spectroscopy such as CF levels of Eu^{3+} in ZnO nanocrystals has ever been documented. To determine the CF levels of Eu^{3+} at multiple sites, the 10 K site-selective excitation and emission spectra of Eu^{3+}:ZnO (1.05 atom %) annealed at 400 °C were measured and shown in Figure 3 and Figures S3−4 (Supporting Information). Compared to that of Eu^{3+}:ZnO (1.6

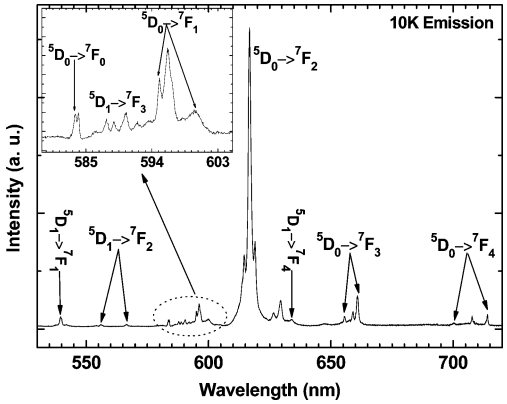

Figure 3. 10 K site-selective emission spectra of the Eu^{3+}:ZnO (1.05 atom %) nanocrystals annealed at 400 °C under the 467.8 nm excitation for Eu^{3+} at site B.

atom %), sites A and B of Eu^{3+} were better resolved from each other in the lower doping sample (1.05 atom %). The surface site (site A) exhibits inhomogeneously broadened excitation and emission line patterns of Eu^{3+} owing to the very distorted local environment (Figures S3a and S4 in the Supporting Information). The lattice site (site B) shows very sharp and intense excitation and emission peaks due to the well crystalline surrounding of Eu^{3+} ions (Figure S3b in the Supporting Information). Figure 3 shows the 10 K site-selective emission spectra under the excitation at 467.8 nm, which correspond to the $^7F_0 \rightarrow {}^5D_2$ transition of Eu^{3+} at the lattice site. The inset of Figure 3 indicates that two close peaks centered at 583.4 and 583.8 nm can be resolved in the region of $^5D_0 \rightarrow {}^7F_0$, which suggests that strictly two lattice sites exist in the ZnO lattice. Consistently, two neighboring peaks centered at 583.5 and 583.9 nm were also resolved in the excitation spectrum of site B by enlarging the region of $^7F_0 \rightarrow {}^5D_0$ (inset of Figure S3, Supporting Information). However, the energy levels of these two sites are so close that we cannot distinguish them in any other regions under the current experimental conditions. In addition to the very sharp $f-f$ transitions attributed to $^5D_0 \rightarrow {}^7F_J$ ($J = 0,1,2,3,4$), weak emission lines of $^5D_1 \rightarrow {}^7F_J$ ($J = 1,2,3,4$) transitions are also detected at 10 K and identified in Figure 3. Note that the

TABLE 1: Partial Energy Levels of Eu^{3+} at Sites A and B in ZnO Nanocrystals at 10 K

multiplet	site A	site B
$^7F_0$	0	0
$^7F_1$	299	318
	369	351
	446	452
$^7F_2$	993	851
		909
		969
		1162
		1238
$^7F_3$	1887	1882
		1931
		1961
		2003
$^7F_4$	2713	2844
	2921	2994
		3118
$^5D_0$	17 271	17 135
$^5D_1$	19 001	18 880
$^5D_2$	21 515	21 292
		21 377
		21 406
$^5D_3$		24 195
$^5L_6$	25 368	24 616
		25 027
		25 162

emissions from $^5D_1$ of Eu^{3+} had never been reported before for Eu^{3+}:ZnO nanocrystals.

On the basis of the high-resolution emission and excitation spectra at 10 and 295 K, we are able to locate and assign some CF levels of Eu^{3+} at both sites, that is, a total number of 12 for site A and 25 for site B, as listed in Table 1. An average energy level for the nondegenerate $^5D_0$ of site B is used. Compared to the surface site, the $^5D_0$ level (17135 cm^{-1}) is found red-shifted for Eu^{3+} at the lattice site (site B). This phenomenon can be well-interpreted by the nephelauxetic (or electron cloud expansion) effect.[33] It is likely that a stronger Eu−O bond for Eu^{3+} at the lattice site results in larger nephelauxetic effect, which thus decreases the interelectronic repulsion of Eu^{3+}. This is reflected by the smaller values of the Slater integrals (or Racah parameters) that cause the red-shift of the $^5D_0$ level. The short bond length and low coordination number may also indicate an enhanced covalency between metal and ligands. Frey and Horrocks revealed that the nephelauxetic effect in Eu^{3+} depends on the covalency of the metal−ligand bond and on the coordination number (the lower the coordination number, the larger the nephelauxetic effect).[34] Similarly, as will be shown later, a shorter bond length and lower coordination number of O atoms were observed for Eu^{3+} ions at site B.

Currently, it is of technical difficulty to perform reliable CF calculations for sites A or B because of the low site symmetries and few experimental levels. However, compared to the centers of gravity of multiplets reported for Eu^{3+}:LaF_3[35] or Eu^{3+}:Gd_2O_3,[36] no significant difference was observed for sites A or B, which indicates similar free-ion parameters between them. A comparison of the CF splitting of $^7F_1$ of both sites shows a relatively strong rank-2 CF strength for site A.

3.3. Local Structure of Eu^{3+}. It is well known that the $^5D_0 \rightarrow {}^7F_2$ transition of Eu^{3+} is of electric-dipole (ED) nature and very sensitive to site symmetry, while the $^5D_0 \rightarrow {}^7F_1$ transition is of magnetic-dipole (MD) nature and insensitive to site symmetry. According to the JO theory,[37,38] the former is permitted on the condition that Eu^{3+} ions occupy a site without an inversion center. The intensity ratio of the $^5D_0 \rightarrow {}^7F_2$ transition to the $^5D_0 \rightarrow {}^7F_1$ transition of Eu^{3+} may provide structural information such as distortion of the ligand environment and site symmetry. In Figure 3, the intensity of the $^5D_0 \rightarrow {}^7F_2$ transition of Eu^{3+} at site B is much stronger than that of the $^5D_0 \rightarrow {}^7F_1$ transition, indicating that Eu^{3+} ions locate at a low-symmetry site without inversion center. Moreover, the $^5D_0 \rightarrow {}^7F_0$ transition of Eu^{3+} at site B induced by CF J-mixing is present in the emission spectrum, which is allowed only for the following 10 site symmetries, C_s, C_1, C_2, C_3, C_4, C_6, C_{2v}, C_{3v}, C_{4v}, and C_{6v} because they possess linear CF components, according to the ED selection rule.[39,40] In hexagonal wurtzite structure, Zn^{2+} ions sit at a C_{3v} lattice site. However, in the present case, the substitution of Zn^{2+} with larger Eu^{3+} ions induces significant lattice distortion. Theoretically, the distortion may descend the original C_{3v} symmetry to C_3, C_s, or C_1 according to the branching rules of the 32 point groups.[41] The three lines we observed for $^5D_0 \rightarrow {}^7F_1$ and five lines for $^5D_0 \rightarrow {}^7F_2$ transitions of Eu^{3+} at site B (Figure 3 and Table 1) suggest C_s or C_1 site symmetry for site B. Besides, the much smaller Li^+ ions may enter the interstitials or substitute for Zn^{2+} in the ZnO lattice to maintain the charge balance between Li^+ and Eu^{3+},[5,8] which will also lower the site symmetry from C_{3v} to C_s (or C_1). In brief, the actual symmetry of site B could be reduced to C_s (or C_1) because of the lattice distortion and charge compensation. For Eu^{3+} at site A, it resides in a glasslike environment (near the surface). Strictly speaking, it should have the lowest site symmetry C_1. Consistently, we observed all three lines for $^5D_0 \rightarrow {}^7F_1$ of Eu^{3+} at site A.

The local structures of Eu^{3+} in ZnO nanocrystals were further investigated by EXAFS spectra. Figure 4 compares the $k^3\chi(k)$ EXAFS spectra of the as-grown (a) and annealed (b) Eu^{3+}:ZnO nanocrystals. The corresponding Fourier transform (FT) data, also shown in Figure 4, reveal intense peaks at ca. 2.0 Å (phase shift uncorrected distance), which are attributable to backscattering from the nearest O atoms about Eu^{3+}. In addition, the FT data reveal weak, distant peaks between 2.5−4.0 Å, which are suggestive of Eu−X (e.g., X ≡ O, Zn, Eu) correlations. The most significant of these features, at 3.7 Å, was shown to arise from Zn backscattering—a result obtained from best-Z search profile fitting of the Eu $k^3\chi(k)$ EXAFS. Quantitative information about the sitting of Eu^{3+} in terms of the nearest Eu−O and distant Eu−Zn interactions—including bond lengths, r, Debye−Waller factors, σ,[2] as well as O and Zn coordination numbers (CNs)—were obtained through curve-fitting analysis. The two-shell fits to the experimental $k^3\chi(k)$ EXAFS are shown as dashed lines in Figure 4. The FTs representing the best fits, also shown as dashed lines, exhibit good correspondence with the primary data (solid lines), thereby confirming that the two-shell model describes the local coordination environment of Eu adequately. The refined, metrical parameters presented in Table 2 show that the O CN and the average Eu−O interatomic distance in the as-grown nanocrystals, 6.8(7) and 2.42(1) Å, respectively, are somewhat larger than those in the annealed sample, 6.0(7) and 2.41(1) Å, respectively. The average Eu−Zn interatomic distances, 3.96(2) and 3.97(2) Å, are essentially equivalent for the as-grown and annealed materials, respectively, whereas the corresponding Zn CNs, 1.4(5) and 0.4(2), exhibit a more significant difference. In general, the differences between the metrical results are consistent with structural variations between lattice and surface sites that are fractionally populated by Eu^{3+} ions. For example, Eu^{3+} occupancy at surface sites, such as is probable for the as-grown material, is expected to have a larger O CN and Eu−O distance than those for Eu^{3+} occupancy in lattice sites, such as is probable for the annealed material, as a result of OH^- adsorption and bond relaxation.

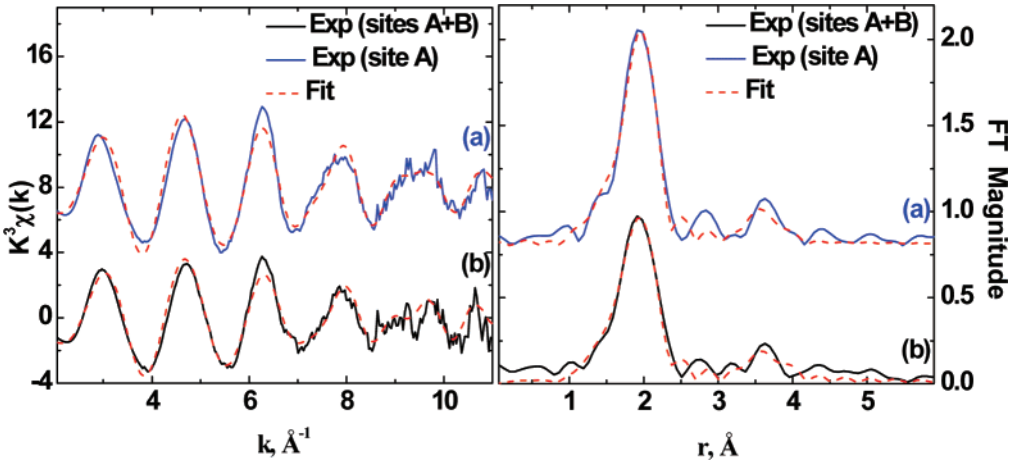

Figure 4. Eu L_3-edge fluorescence EXAFS for Eu^{3+}:ZnO (1.05 atom %) nanocrystals, (a) as-grown, and (b) annealed at 400 °C. The experimental $k^3\chi(k)$ spectra (left panel) and the corresponding FT data (right panel, without phase shift correction) are shown as solid lines. The best fits obtained with a seven-parameter, two-shell (Eu−O, Eu−Zn) model are shown as dashed lines in both the left and right panels. The resulting metrical parameters are given in Table 2.

TABLE 2: Metrical Results Obtained from the Curve-Fitting Analysis of the Eu L_3-Edge $k^3\chi$(k) EXAFS Data for Eu^{3+}:ZnO Nanocrystals[a]

sample	bond type	r (Å)	CN	σ^2 (Å^2)	ΔE (eV)	site type
as-grown	Eu−O	2.42(1)	6.8(7)	0.009(1)	0.9(3)	site A
	Eu−Zn	3.96(2)	1.4(5)	0.008(3)	0.9(3)	
annealed	Eu−O	2.41(1)	6.0(7)	0.011(2)	1.5(3)	sites A + B
	Eu−Zn	3.97(2)	0.4(2)	0.001(1)	1.5(3)	

[a] Estimated standard deviations shown in parentheses are the 95% confidence limits obtained from the diagonal elements of the covariance matrix of the least-squares fits.

Indeed, the EXAFS results for the Eu^{3+}:ZnO nanocrystals annealed at 400 °C reveal a smaller O CN of 6 and, yet, the average Eu−O bond length, 2.41(1) Å, is 0.43 Å longer than the Zn−O bond length (1.98 Å) in undoped ZnO, thereby suggesting a substantial extent of lattice distortion around Eu^{3+}, more so than can be accounted for by the difference (0.207 Å) between the ionic radii of Eu^{3+} and Zn^{2+} alone, 0.947 and 0.74 Å, respectively, for CN = VI.[42] It should be noted that the Eu EXAFS response provides an average coordination environment of all of the Eu^{3+} ions in the ZnO nanocrystals. As such, the 6 O coordination of Eu in the 400 °C-annealed Eu^{3+}:ZnO nanocrystals is an average result for both site A (CN ≈ 7, Table 2) and site B (CN = 4, presumably for the tetragonal lattice site). To better probe the local structure of Eu^{3+} ions in the ZnO lattice, Eu^{3+}:ZnO nanocrystals in which Eu occupies a single lattice site (site B) are required for EXAFS experiments. The synthesis of such single-site Eu^{3+}:ZnO nanocrystals is still under way. It is important to realize that, in comparison to the EXAFS results with the optical spectra that clearly distinguish the lattice site and the surface sites, a small difference in local structure would lead to significant changes in the electronic energy levels and the excited-state dynamics of the doped ions. Therefore, from the viewpoint of spectroscopy, the interplay of structure distortion and the ion−lattice electronic interaction becomes more significant for RE ions in semiconductors than that in dielectric crystals.

3.4. Luminescence Lifetime. To reveal the CF environment experienced by Eu^{3+} at multiple sites, we measured the luminescence lifetimes of Eu^{3+} at sites A and B in Eu^{3+}:ZnO (1.05 atom %) nanocrystals annealed at 400 °C by monitoring the site-selective emission ($^5D_0 \rightarrow {}^7F_2$) at 10 K. As shown in Figure 5, the decay curve from $^5D_0$ of Eu^{3+} at site B shows a noticeable rising edge at the initial stage and a single-exponential decay in the tail when excited to the $^5D_2$ state. The intrinsic lifetime of the $^5D_0$ can be determined to be 1.25 ms from the tail at 10 K. Meanwhile, the lifetime of $^5D_1$ is determined to be ~56 μs at 10 K according to the rising edge of the $^5D_0$ decay curve (inset of Figure 5).[43] Different from site B, the $^5D_0$ decay of site A exhibits a single-exponential decay without a rising edge (Figure 5). The $^5D_0$ lifetime of site A is determined to be 0.75 ms, much shorter than that of site B. The absence of the rise time and the shorter lifetime are expected for the surface site (A) because the surface defects or impurity ligands such as OH^- in nanocrystals might act as the channels of nonradiative relaxation, thus inducing rapid nonradiative transition for $^5D_1 \rightarrow {}^5D_0$ and the shorter lifetime of $^5D_0$.

The luminescence lifetime of $^5D_0$ of Eu^{3+} in ZnO nanocrystals is observed to be weakly dependent on the temperature. The $^5D_0$ lifetime of sites A and B are determined to be 0.69 and 1.05 ms by monitoring the site-selective emission ($^5D_0 \rightarrow {}^7F_2$) at room temperature (RT), respectively. Thus, the observed lifetime of $^5D_0$ of Eu^{3+} can be approximately regarded as the radiative lifetime in view of the large energy gap between $^5D_0$ and its next low-lying $^7F_6$ (~12000 cm^{-1}). There are many factors that may influence the radiative lifetime of $^5D_0$ of Eu^{3+} in nanocrystals such as the non-solid surrounding media and changes of the lattice constants.[44−46] As shown in the following, the non-solid medium surrounding the nanocrystals that changes the effective index of refraction (n_{eff}) may have significant impact on the $^5D_0$ lifetime of Eu^{3+} in ZnO nanocrystals. The dependence of the radiative lifetime τ_r on the index of refraction n can be described with the virtual-cavity model (which is based on the Lorentz local field) by the following equation[45,47,48]

$$\tau_r \sim \frac{1}{f}\frac{\lambda_0^2}{\chi} \qquad (1)$$

where $\chi = [1/3(n^2 + 2)]^2 n$ for the ED transition and $\chi = n^3$ for the MD transition; f is the oscillator strength for transitions in vacuum; λ_0 is the wavelength in vacuum; n is the refractive index of the medium. For nanocrystals with a size much smaller than the wavelength of light, n should be replaced by an effective index of refraction (n_{eff}). The effective index of refraction (n_{eff}) is defined as $n_{eff} = xn_{np} + (1 - x)n_{med}$, where x is the filling factor showing what fraction of space is occupied by the nanocrystals with a refractive index of n_{np} (2.0039 for ZnO),[49] and n_{med} is the refractive index of the medium. We have

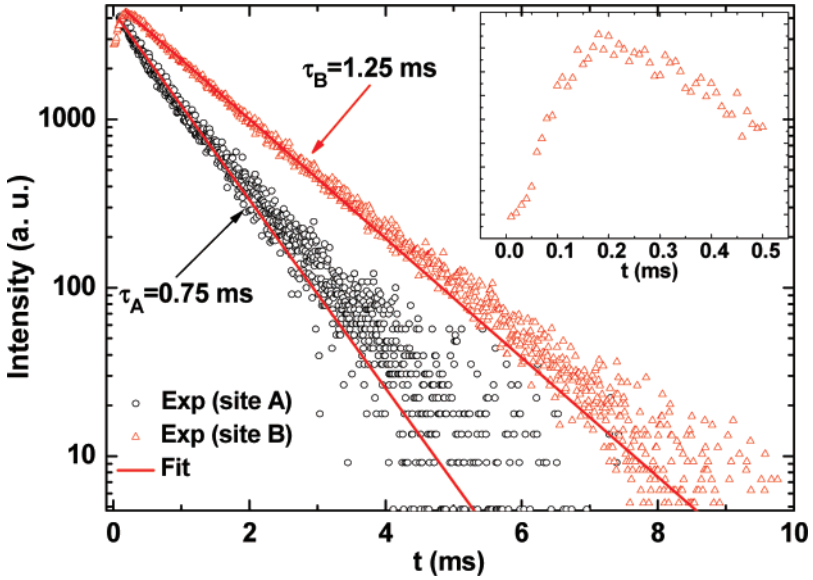

Figure 5. 10 K fluorescence decays from $^5D_0$ of Eu^{3+} at sites A and B under the site-selective excitation at 464.8 and 467.8 nm, respectively. The inset shows the initial rise time due to the decay from $^5D_1$ of Eu^{3+} at site B.

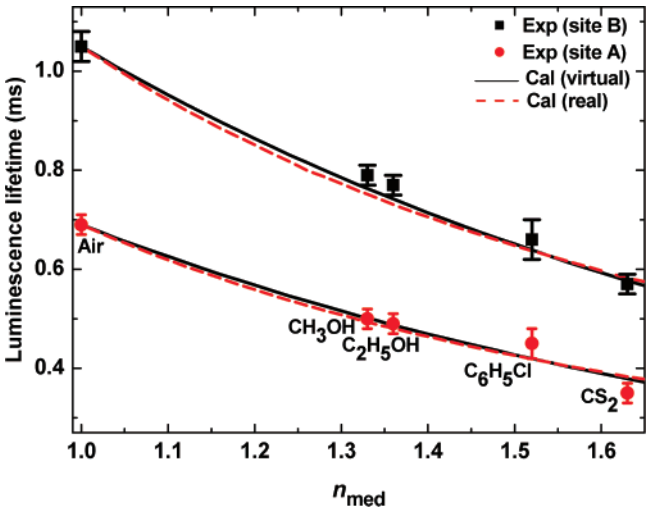

Figure 6. Dependence of the $^5D_0$ lifetimes of Eu^{3+} at sites A and B in Eu^{3+}:ZnO (1.05 atom %) nanocrystals on the refractive index of the medium at room temperature. The scattering points are the observed data, whereas the solid (and dashed) lines are the fitting results with the virtual- (and real-) cavity models, respectively.

measured the $^5D_0$ lifetimes of Eu^{3+} at sites A and B in ZnO nanocrystals being immersed in solvents with different refractive indices. The media included methanol (CH_3OH, $n = 1.329$), ethanol (C_2H_5OH, $n = 1.361$), carbon disulfide (CS_2, $n = 1.628$), and chlorobenzene (C_6H_5Cl, $n = 1.525$). Figure 6 shows the dependence of the measured $^5D_0$ lifetimes of Eu^{3+} on the refractive index of the medium (n_{med}) at RT. The experimental data for both sites A and B have been used for fitting with eq 1, using x as an adjustable parameter. It was found that a filling factor of 0.52 gave an optimal fit for both sites A and B. The fact that the same filling factor was determined for both sites A and B is a good indication that this fitting model is a valid one. A similar fitting was also performed successfully for the C_2 and C_{3i} sites of Eu^{3+} in Lu_2O_3 nanocrystals.[48] The larger index of refraction of the surrounding medium leads to the smaller radiative lifetime. The $^5D_0$ lifetimes of Eu^{3+} in bulk ZnO for sites A and B can be estimated to be 0.27 and 0.41 ms by the extrapolation of abscissa n_{med} to n_{bulk} (ZnO, 2.0039) at RT, respectively, although the observed values are not available in the literature. Thus, it is firmly established that the longer radiative lifetime of $^5D_0$ of Eu^{3+} in ZnO nanocrystals is mainly due to the non-solid surrounding medium that changes the effective index of refraction.

Interestingly, the dependence of the luminescence lifetime on the refractive index can be also interpreted with another model, that is, the real-cavity model, where emitters are assumed to create tiny cavities when replacing host ions, which has been performed successfully for Eu^{3+}−ligand complexes in different liquids[50] and in a supercritical CO_2 gas as a function of pressure.[51] Specifically, Duan and Reid recently re-fitted the measured lifetimes for Y_2O_3:Eu^{3+} nanoparticles immersed in different solvents and showed that the real-cavity model is also applicable for the lifetime dependence on the refractive index, in addition to the widely used virtual-cavity model.[52,53] For comparison, we performed a similar fitting procedure for Eu^{3+}:ZnO nanocrystals with the real-cavity model by the following formula[52,53]

$$\tau_R \sim \tau_{bulk} \frac{1}{n_r} \left(\frac{2n_r^2 + 1}{3n_r^2} \right)^2 \quad (2)$$

where $n_r = n_{eff}/n_{np}$, τ_{bulk} is denoted as the lifetime of bulk Eu^{3+}:ZnO, and n_{eff} is the effective index of refraction aforementioned. We re-fitted the experimental data with eq 2. It turned out, for Eu^{3+}:ZnO nanocrystals immersed in different solvents, that the fitting results (filling factor, $x = 0.45$) could be comparable to that of the virtual-cavity model, as shown in Figure 6. Although the difference between two models is very small in Figure 6, the real-cavity model gives a relatively larger root-mean-square deviation (~0.032) for the fitting compared to that of the virtual-cavity model (~0.025). In other words, the virtual-cavity model (solid lines) results in a slightly better fit for both sites A and B in Eu^{3+}:ZnO nanocrystals.

3.5. Judd−Ofelt Intensity Calculation. The JO intensity parameters $\Omega_{2,4,6}$ of Eu^{3+} at sites A and B in ZnO nanocrystals can be calculated directly using the method proposed by Krupke[54] and subsequently used by others.[48,55] This method takes advantage of the fact that the intensities of the $^5D_0 \rightarrow {}^7F_2$, $^5D_0 \rightarrow {}^7F_4$, and $^5D_0 \rightarrow {}^7F_6$ transitions are solely dependent on the Ω_2, Ω_4, and Ω_6 parameters, respectively. Because the radiative transition rate is proportional to the integrated intensity

TABLE 3: JO Intensity Parameters of Eu^{3+} Ions in Different Hosts (in Units of 10^{-20} cm^2)

host	Ω_2	Ω_4	Ω_6	ref
Eu^{3+} (aquo)	1.62	5.65	5.02	60
ZBLAN (glass)	2.89	3.87	2.88	56
LaF_3 (crystal)	1.19	1.16	0.39	61
$YAlO_3$ (crystal)	2.66	6.33	0.80	62
Y_2O_3 (crystal)	9.86	2.23	<0.32	55
Gd_2O_3 (nano)	12.39	2.02	0.19	36
ZnO (nano)	9.59	8.11	<0.25	site A
	21.51	2.30	<0.25	site B

of the transition band in the emission spectrum (i.e., $A(J \rightarrow J') \propto \int \lambda I_{J'}(\lambda)\, d\lambda$), the radiative transition rate of $^5D_0 \rightarrow {}^7F_J$ ($J = 0, 2-6$) can be estimated according to the ratio of the integrated intensity of $^5D_0 \rightarrow {}^7F_1$ to these transitions. The calculated radiative transition rate of $^5D_0 \rightarrow {}^7F_1$, which is of MD nature and insensitive to the site symmetry, is used as a reference to scale the absolute ED transition rates of $^5D_0 \rightarrow {}^7F_J$ ($J = 2,4,6$) by

$$A_{MD}(J \rightarrow J') = \frac{64\pi^4 e^2 n^3}{3h(2J+1)\bar{\lambda}^3}\left(\frac{e\hbar}{2mc}\right)^2 |\langle \Phi J||L + 2S||\Phi' J'\rangle|^2 \quad (3)$$

where n is the effective index of refraction for the nanocrystals as discussed in Section 3.4; $\bar{\lambda}$ is the mean wavelength of the emission band; $|\langle \Phi J||L + 2S||\Phi' J'\rangle|^2$are the reduced matrix elements (RMEs) of the MD operator, which were calculated based on the intermediate-coupling wave functions. Once the ED radiative transition rates of $^5D_0 \rightarrow {}^7F_J$ ($J = 2,4,6$) are determined, the JO intensity parameters $\Omega_{2,4,6}$ can be calculated using the following formula

$$A_{ED}(J \rightarrow J') = \frac{64\pi^4 e^2}{3h(2J+1)\bar{\lambda}^3}\frac{n(n^2+2)^2}{9} \sum_{t=2,4,6} \Omega_t |\langle \Phi J||U^{(t)}||\Phi' J'\rangle|^2 \quad (4)$$

where $|\langle \Phi J||U^{(t)}||\Phi' J'\rangle|^2$ are the RMEs of the unit tensor. The RME data of the unit tensor and the MD operator are taken from those values of Eu^{3+}:Gd_2O_3[36] because they are insensitive to the host. According to the emission spectra (Figures 3 and S4), the JO intensity parameters $\Omega_{2,4}$ were determined to be 9.59, 8.11 for Eu^{3+} at site A, and 21.51, 2.30 for Eu^{3+} at site B in units of 10^{-20} cm^2. The transition of $^5D_0 \rightarrow {}^7F_6$ proved to be too weak to detect in our experimental setup, so a value for Ω_6 could not be determined. It can be inferred from the known minimum detectable power of the system that Ω_6 must be less than 2.5×10^{-21} cm^2. Table 3 compares the JO parameters of Eu^{3+} in different hosts such as aquo, glass, crystal, and nanocrystal. The very small Ω_6 of Eu^{3+}:ZnO, similar to that of $YAlO_3$, Y_2O_3 and Gd_2O_3, is presumably ascribed to the relatively small fifth- and seventh-order CF components.[37,54] The values of $\Omega_{2,4}$ for Eu^{3+} at site B are significantly different from that for Eu^{3+} at site A, which verifies the different CF environments experienced by Eu^{3+} at different sites. Particularly, for Eu^{3+} at site B, the value of Ω_2 reaches 21.51×10^{-20} cm^2. The variation of Ω_2, reflected by the hypersensitivity of the $^5D_0 \rightarrow {}^7F_2$ transition, can be related to a variation in the covalency of the Eu−O bond as well as in the structural environment around Eu^{3+} ions.[56] The large value of Ω_2 for Eu^{3+} at site B may suggest an enhanced covalency or shorter bond length between the trivalent Eu and oxide anions and a relatively low site symmetry of Eu^{3+}. This effect is consistent with the significant red-shift of $^5D_0$, as discussed already in Sections 3.2−3.3. For Eu at site B, the smaller O CN number and shorter bond length could result in a large nephelauxetic effect and large Ω_2 value.

3.6. Host-to-Eu^{3+} Energy Transfer. The host-to-RE energy transfer plays an important role in improving the emission efficiency for the solid-state luminescence materials. For Eu^{3+}:ZnO nanophosphors, the europium activator is expected to be sensitized by the exciton recombination, which leads to an energy transfer from ZnO host to Eu^{3+} ions, thus producing a bright-red luminescence of Eu^{3+} ions. In the excitation spectra of Eu^{3+}:ZnO nanocrystals annealed at 400 °C (Figure S3 in Supporting Information), we can observe a broad excitation band centered at ∼369 nm, which is attributed to the band gap excitation and defects of ZnO nanocrystals.[20,57] The strong broad excitation peak suggests that a host-to-Eu^{3+} energy transfer took place. The 10 K emission spectrum under the 369 nm excitation shows the typical Eu^{3+} luminescence of major site B plus other minor sites superimposed on a wide orange band (peaking at ∼600 nm) due to defects of excess oxygen (Figure 7). Therefore, it can be inferred that more efficient energy transfer from the host to site B occurs, which is most likely due to better energy matching between Eu^{3+} at site B and the host. This energy transfer plus the lack of emission from site A further confirms that site A is likely close to the surface, whereas site B should be embedded in the ZnO lattice. It should be noted that such host-to-Eu^{3+} energy transfer was not observed for Eu^{3+} doped ZnS nanocrystals because of energy mismatch between Eu^{3+} ions and the ZnS host.[13] To investigate the mechanism of energy transfer from the ZnO host to Eu^{3+} ions, we have measured the 10 K luminescence decay by monitoring the strongest $^5D_0 \rightarrow {}^7F_2$ transition of Eu^{3+} (616.8 nm, site B) under the band gap excitation. As shown in the inset of Figure 7, the decay curve fits well to a single exponential, and the lifetime is determined to be approximately 1.28 ms, in good agreement with the value obtained under the direct excitation of Eu^{3+} ions at site B. However, no rising edge is observed at the initial stage in the decay curve of $^5D_0$, which is very different from that under the direct excitation of Eu^{3+}. Besides, no $^5D_1 \rightarrow {}^7F_J$ ($J = 1,2,3,4$) emissions of Eu^{3+} were observed under the band gap excitation. The vanishing of the rising edge and the emissions from $^5D_1$ of Eu^{3+} suggest that an energy transfer from the ZnO host to the $^5D_0$ state of Eu^{3+} ions might take place. In this process, defect states may act as the intermediate channels to assist the energy transfer between ZnO and Eu^{3+} ions. Various types of defect states have been shown to play an important role in energy transfer between semiconductors (such as TiO_2) and RE ions.[58,59] Ishizumi and Kanemitsu have observed an energy transfer from ZnO nanorods to Eu^{3+} through the defects of ZnO nanorods; nevertheless, the excitation energies therein were lower than the band gap energy of ZnO.[15] On the basis of the photoluminescence (PL) and PL decay of Eu^{3+} ions under the band gap excitation, a possible mechanism for the energy transfer from ZnO band gap to Eu^{3+} ions is proposed and depicted in Figure 8. Under the band gap excitation, excitation light is absorbed by the ZnO nanocrystals that leads to the creation of an exciton. The exciton recombination would transfer its energy to the excited state of the defects, followed by an energy transfer to the $^5D_0$ state of Eu^{3+} ions via a nonradiative relaxation process, and then the radiative relaxation from $^5D_0$ to ${}^7F_J$ ($J = 0,1,2,3,4$) occurs. Note that the radiative emission from the defects characterized by a broad orange band is also observed, which somewhat limits the efficiency of the host-to-Eu^{3+} energy transfer as well as the intensity of red luminescence of Eu^{3+}.

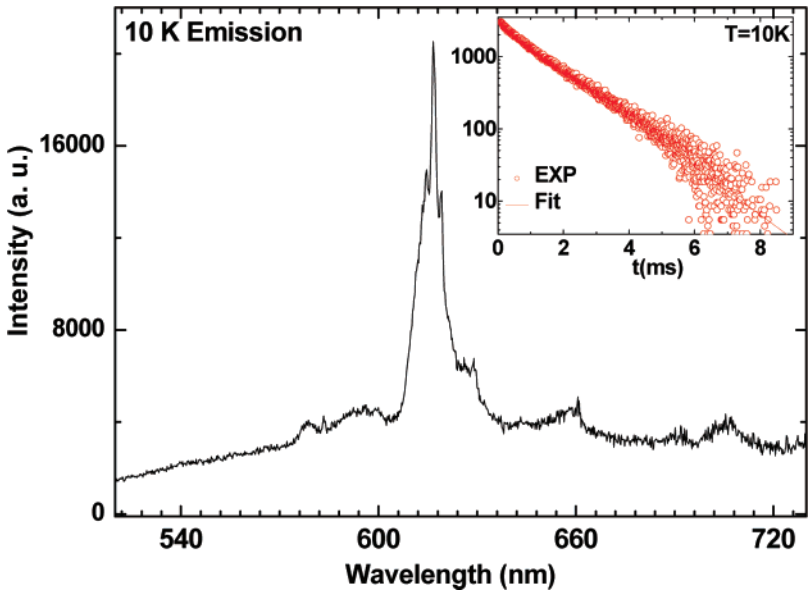

Figure 7. 10 K emission spectrum of Eu^{3+}:ZnO (1.05 atom %) nanocrystals annealed at 400 °C under 369 nm excitation. The inset is the 10 K fluorescence decay from $^5D_0$ of Eu^{3+}under the excitation at 369 nm.

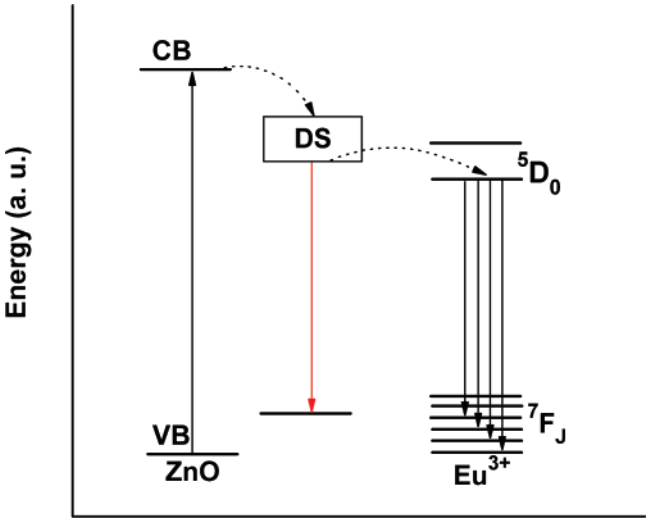

Figure 8. Schematic illustration showing the possible mechanism of energy transfer from ZnO host to Eu^{3+}. VB, CB, and DS are the abbreviations of valence band, conduction band, and defect states, respectively.

Currently, we are finding ways to improve this energy transfer efficiency, for instance, by co-doping of other RE ions such as Tb^{3+} ions, which act as a bridge in transferring the energy absorbed by the host to Eu^{3+}.

3.7. Growth Mechanism for the Incorporation of Eu^{3+} Ions into the ZnO Lattice. Finally, an important issue that needs to be addressed is the following: Why it is difficult to incorporate Eu^{3+} ions into the nanocrystals if annealing the as-grown sample above 500 °C? On the basis of the XRD, TEM, and PL spectra, a plausible mechanism for the incorporation of Eu^{3+} ions in ZnO nanocrystals is proposed and depicted in Figure 9. First of all, by refluxing the mixture of zinc acetate dihydrate, europium acetate hexahydrate, and absolute ethanol under vigorous stirring in an 80 °C water bath, −Zn−O−Eu− and −Zn−O−Zn− precursors were obtained in the solution similar to the previous reports.[9,14,18,19,22] The hydrolysis by addition of lithium hydroxide monohydrate powder in an ultrasonic bath at 0 °C resulted in the formation of ZnO nanoparticles with their surfaces covered with Eu^{3+}, Li^+, and hydroxyls. It has been confirmed by spectroscopic evidence that

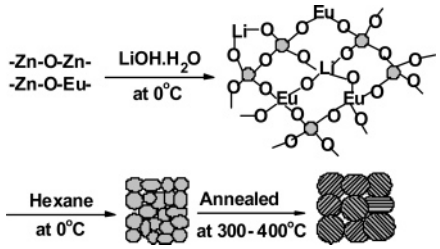

Figure 9. Schematic illustration showing the growth mechanism of Eu^{3+} doped ZnO nanocrystals.

only site A (surface site) was formed in the as-grown nanoparticles. After the addition of hexane, ZnO nanoparticles were precipitated from the sol−gel solution, as observed in Figure 1a. By annealing at 300−400 °C, two or more ZnO nanoparticles would be merged into one single wurtzite nanocrystal in the crystallization process (Figure 1b and c). As a consequence, some Eu^{3+} ions sitting in the interfaces or grain boundaries between nanoparticles might enter the Zn lattice to lower the interfacial energy of the nanoparticles. In other words, some Eu^{3+} ions at site A can be transformed to site B during the crystallization process. Because of the lattice distortion and charge compensation of Li^+ ions, multiple sites of Eu^{3+} incorporated in the ZnO lattice were formed. However, owing to the very different chemical properties between Zn^{2+} and Eu^{3+} ions, the substitution may be thermally unstable. Eu^{3+} ions at the lattice site are prone to be expelled from the ZnO matrix during the nanocrystal growth at higher annealing temperatures (above 500 °C). For instance, when the as-grown sample was annealed at 500 °C, no lattice site was detected. Instead, a small amount of the Eu_2O_3 impurity phase was formed, as can be identified by XRD (Figure S5 in the Supporting Information).

4. Conclusions

In summary, the spectroscopic and optical properties of Eu^{3+} at the surface and lattice sites of ZnO nanocrystals, including energy levels, local structures, JO parameters, PL lifetimes, and host-to-RE energy transfer have been investigated and compared extensively. As a result of lattice distortion and enhanced covalency of the Eu−O bond, a significant red-shift of $^5D_0$ and large Ω_2 parameters were observed for Eu^{3+} at the lattice site.

The lifetimes of Eu^{3+} at the lattice and surface sites were simultaneously affected by the non-solid surrounding medium, which can be better interpreted with the virtual-cavity model compared to the real-cavity model. The host-to-Eu^{3+} energy transfer is found to occur from the ZnO band gap to the $^5D_0$ state of Eu^{3+} via the intermediate defect states. Deep insight into these novel optical properties of Eu^{3+}:ZnO nanophosphors, particularly the host-to-Eu^{3+} energy transfer, is of great importance to material applications such as the fabrication of electroluminescence devices and biolabels. It is anticipated that similar syntheses and analyses can be extended to other RE ions doped semiconductor nanomaterials.

Acknowledgment. This work is supported by the One Hundred Talents Program of the Chinese Academy of Sciences, the NSFC (Grant Nos. 10504032 and 10774143), the 973 program (No. 2007CB936703), the Startup Foundation from the State Ministry of Personnel of China, and the Science and Technology Foundation of Fujian Province (Nos. 2006F3137 and 2007I0024). Work at Argonne National Laboratory (ANL) was supported by the U.S. Department of Energy, Office of Basic Energy Sciences, Division of Chemical Sciences, Geosciences, and Biosciences, under contract DE-AC02-06CH11357. We thank the staff of Advanced Photon Source beam line 12-BM-M at ANL for EXAFS experiments.

Supporting Information Available: XRD patterns of Eu^{3+}:ZnO nanoparticles annealed at different temperatures; PL intensity of Eu^{3+} doped ZnO nanocrystals as a function of the Eu^{3+} content; the 10 K excitation spectra of Eu^{3+}:ZnO nanocrystals by monitoring the $^5D_0$-$^7F_2$ emission of Eu^{3+}; the 10 K site-selective emission spectra of Eu^{3+}:ZnO nanocrystals under the 464.8 nm excitation for Eu^{3+} at site A; and XRD patterns of Eu^{3+}:ZnO nanoparticles annealed at 500 °C. This material is available free of charge via the Internet at http://pubs.acs.org.

References and Notes

(1) Yanes, A. C.; Del Castillo, J.; Torres, M.; Peraza, J.; Rodriguez, V. D.; Mendez-Ramos, J. *Appl. Phys. Lett.* **2004**, *85*, 2343.

(2) Qu, S. C.; Zhou, W. H.; Liu, F. Q.; Chen, N. F.; Wang, Z. G.; Pan, H. Y.; Yu, D. P. *Appl. Phys. Lett.* **2002**, *80*, 3605.

(3) Bang, J.; Yang, H.; Holloway, P. H. *J. Chem. Phys.* **2005**, *123*, 084709.

(4) Conde-Gallardo, A.; Garcia-Rocha, M.; Hernandez-Calderon, I.; Palomino-Merino, R. *Appl. Phys. Lett.* **2001**, *78*, 3436.

(5) Zhou, Z.; Komori, T.; Ayukawa, T.; Yukawa, H.; Morinaga, M.; Koizumi, A.; Takeda, Y. *Appl. Phys. Lett.* **2005**, *87*, 091109.

(6) Liu, Q. L.; Bando, Y.; Xu, F. F.; Tang, C. C. *Appl. Phys. Lett.* **2004**, *85*, 4890.

(7) Chen, L.; Zhang, J.; Lu, S.; Ren, X.; Wang, X. *Chem. Phys. Lett.* **2005**, *409*, 144.

(8) Gu, F.; Wang, S. F.; Lu, M. K.; Zhou, G. J.; Xu, D.; Yuan, D. R. *Langmuir* **2004**, *20*, 3528.

(9) Schmidt, T.; Muller, G.; Spanhel, L.; Kerkel, K.; Forchel, A. *Chem. Mater.* **1998**, *10*, 65.

(10) Armelao, L.; Heigl, F.; Jurgensen, A.; Blyth, R. I. R.; Regier, T.; Zhou, X.-T.; Sham, T. K. *J. Phys. Chem. C* **2007**, *111*, 10194.

(11) Erwin, S. C.; Zu, L. J.; Haftel, M. I.; Efros, A. L.; Kennedy, T. A.; Norris, D. J. *Nature* **2005**, *436*, 91.

(12) Galli, G. *Nature* **2005**, *436*, 32.

(13) Bol, A. A.; van Beek, R.; Meijerink, A. *Chem. Mater.* **2002**, *14*, 1121.

(14) Wang, X.; Kong, X. G.; Shan, G. Y.; Yu, Y.; Sun, Y. J.; Feng, L. Y.; Chao, K. F.; Lu, S. Z.; Li, Y. J. *J. Phys. Chem. B* **2004**, *108*, 18408.

(15) Ishizumi, A.; Kanemitsu, Y. *Appl. Phys. Lett.* **2005**, *86*, 253106.

(16) Ishizumi, A.; Taguchi, Y.; Yamamoto, A.; Kanemitsu, Y. *Thin Solid Films* **2005**, *486*, 50.

(17) Pereira, A. S.; Peres, M.; Soares, M. J.; Alves, E.; Neves, A.; Monteiro, T.; Trindade, T. *Nanotechnology* **2006**, *17*, 834.

(18) Liu, S. M.; Liu, F. Q.; Wang, Z. G. *Chem. Phys. Lett.* **2001**, *343*, 489.

(19) Liu, S. M.; Liu, F. Q.; Guo, H. Q.; Zhang, Z. H.; Wang, Z. G. *Phys. Lett. A* **2000**, *271*, 128.

(20) Liu, Y. S.; Luo, W. Q.; Li, R. F.; Chen, X. Y. *Opt. Lett.* **2007**, *32*, 566.

(21) Spanhel, L.; Anderson, M. A. *J. Am. Chem. Soc.* **1991**, *113*, 2826.

(22) Meulenkamp, E. A. *J. Phys. Chem. B* **1998**, *102*, 5566.

(23) Beno, M. A.; Engbretson, M.; Jennings, G.; Knapp, G. S.; Linton, J.; Kurtz, C.; Rutt, U.; Montano, P. A. *Nucl. Instrum. Methods Phys. Res., Sect. A* **2001**, *467*, 699.

(24) Liu, G. K.; Zhorin, V. V.; Antonio, M. R.; Li, S. T.; Williams, C. W.; Soderholm, L. *J. Chem. Phys.* **2000**, *112*, 1489.

(25) For documentation and availability see http://www-ssrl.slac.stanford.edu/exafspak.html.

(26) Rehr, J. J.; Albers, R. C. *Rev. Mod. Phys.* **2000**, *72*, 621.

(27) Stern, E. A. *Phys. Rev. B* **1993**, *48*, 9825.

(28) Zeng, Q. G.; Ding, Z. J.; Zhang, Z. M. *J. Lumin.* **2006**, *118*, 301.

(29) Kortum, G. *Reflectance Spectroscopy*; Springer-Verlag: New York, 1969.

(30) Cao, G.; Rabenberg, L. K.; Nunn, C. M.; Mallouk, T. E. *Chem. Mater.* **1991**, *3*, 149.

(31) Wang, Y. S.; Thomas, P. J.; O'Brien, P. *J. Phys. Chem. B* **2006**, *110*, 4099.

(32) Antony, J.; Chen, X. B.; Morrison, J.; Bergman, L.; Qiang, Y.; McCready, D. E.; Engelhard, M. H. *Appl. Phys. Lett.* **2005**, *87*, 241917.

(33) Reisfeld, R. J., C. K. *Lasers and Excited States of Rare Earths*; Springer: Berlin, 1977.

(34) Frey, S. T.; Horrocks, W. D. *Inorg. Chim. Acta* **1995**, *229*, 383.

(35) Carnall, W. T.; Goodman, G. L.; Rajnak, K.; Rana, R. S. *J. Chem. Phys.* **1989**, *90*, 3443.

(36) Liu, L. Q.; Chen, X. Y. *Nanotechnology* **2007**, *18*, 255704.

(37) Judd, B. R. *Phys. Rev.* **1962**, *127*, 750.

(38) Ofelt, G. S. *J. Chem. Phys.* **1962**, *37*, 511.

(39) Chen, X. Y.; Liu, G. K. *J. Solid State Chem.* **2005**, *178*, 419.

(40) Chen, X. Y.; Zhao, W.; Cook, R. E.; Liu, G. K. *Phys. Rev. B* **2004**, *70*, 205122.

(41) Butler, P. H. *Point Group Symmetry Application: Method and Tables*; Plenum: New York, 1981.

(42) Shannon, R. D. *Acta Crystallogr.* **1976**, *A32*, 751.

(43) Chen, X. Y.; Yang, L.; Cook, R. E.; Skanthakumar, S.; Shi, D.; Liu, G. K. *Nanotechnology* **2003**, *14*, 670.

(44) Liu, G. K.; Chen, X. Y. Spectroscopic Properties of Lanthanides in Nanomaterials. In *Handbook on the Physics and Chemistry of Rare Earths*; Gschneidner, K. A., Jr., Bunzli, J. C. G., Pecharsky, V. K., Eds.; Elsevier Science B.V.: Amsterdam, 2007; Vol. 37, p 99.

(45) Meltzer, R. S.; Feofilov, S. P.; Tissue, B.; Yuan, H. B. *Phys. Rev. B* **1999**, *60*, R14012.

(46) Schmechel, R.; Kennedy, M.; von Seggern, H.; Winkler, H.; Kolbe, M.; Fischer, R. A.; Li, X. M.; Benker, A.; Winterer, M.; Hahn, H. *J. Appl. Phys.* **2001**, *89*, 1679.

(47) Henderson, B.; Imbusch, G. F. *Optical Spectroscopy of Inorganic Solids*; Clarendon Press: Oxford, 1989.

(48) Boyer, J. C.; Vetrone, F.; Capobianco, J. A.; Speghini, A.; Bettinelli, M. *J. Phys. Chem. B* **2004**, *108*, 20137.

(49) Bond, W. L. *J. Appl. Phys.* **1965**, *36*, 1674.

(50) Rikken, G. L. J. A.; Kessener, Y. A. R. R. *Phys. Rev. Lett.* **1995**, *74*, 880.

(51) Schuurmans, F. J. P.; de Lang, D. T. N.; Wegdam, G. H.; Sprik, R.; Lagendijk, A. *Phys. Rev. Lett.* **1998**, *80*, 5077.

(52) Duan, C. K.; Reid, M. F. *J. Alloys Compd.* **2006**, *418*, 213.

(53) Duan, C. K.; Reid, M. F.; Wang, Z. Q. *Phys. Lett. A* **2005**, *343*, 474.

(54) Krupke, W. F. *Phys. Rev.* **1966**, *145*, 325.

(55) Weber, M. J. *Phys. Rev.* **1968**, *171*, 283.

(56) Gorller-Warland, C.; Binnemans, K. Spectral Intensities of f-f Transitions. In *Handbook on the Physics and Chemistry of the Rare Earths*; Gschneidner, K. A., Jr., Eyring, L., Eds.; North-Holland: Amsterdam, 1998; Vol. 25, p 101.

(57) Lima, S. A. M.; Sigoli, F. A.; Davolos, M. R.; Jafelicci, M. *J. Alloys Compd.* **2002**, *344*, 280.

(58) Frindell, K. L.; Bartl, M. H.; Robinson, M. R.; Bazan, G. C.; Popitsch, A.; Stucky, G. D. *J. Solid State Chem.* **2003**, *172*, 81.

(59) Xin, H.; Ma, R. Z.; Wang, L. Z.; Ebina, Y. S.; Takada, K.; Sasaki, T. *Appl. Phys. Lett.* **2004**, *85*, 4187.

(60) Binnemans, K.; VanHerck, K.; GorllerWalrand, C. *Chem. Phys. Lett.* **1997**, *266*, 297.

(61) Weber, M. J. Relaxation processes for excited states of Eu^{3+} in LaF_3. In *Optical Properties of Ions in Crystals*; Crosswhite, H. M., Moos, H. W., Eds.; John Wiley & Sons, Inc.: New York, 1967; p 467.

(62) Weber, M. J.; Varitimos, T. E.; Matsinger, B. H. *Phys. Rev. B* **1973**, *8*, 47.